

Polymer solution with very low relaxation time: a combined numerical-experimental determination strategy

Guillaume Maîtrejean

Laboratoire Rhéologie et Procédés
Univ. Grenoble Alpes, LRP
F-38000 Grenoble France

Maxime Rosello

Laboratoire Rhéologie et Procédés
Univ. Grenoble Alpes, LRP
F-38000 Grenoble France

Email: guillaume.maitrejean@univ-grenoble-alpes.fr

Denis CD Roux

Laboratoire Rhéologie et Procédés
Univ. Grenoble Alpes, LRP
F-38000 Grenoble France

Pascal Jay

Laboratoire Rhéologie et Procédés
Univ. Grenoble Alpes, LRP
F-38000 Grenoble
France

Jean Xing

Markem-Imaje Industries
ZA de l'Armailler 9
rue Gaspard Monge
BP 110 26501 Bourg-Lés-Valence
France

Bruno Barbet

Markem-Imaje Industries
ZA de l'Armailler 9
rue Gaspard Monge
BP 110 26501 Bourg-Lés-Valence
France

ABSTRACT

For very low relaxation time (i.e. lesser than a microsecond) viscoelastic fluid experimental determination is difficult, if not impossible. In the present work the relaxation time measure-

ment of a weakly elastic polymer solution, too low to be measured using classical rheometry techniques, is assessed using a mixed experimental-numerical strategy. First the fluid is rheologically assessed, by measuring its shear viscosity, surface tension and density. Then the relaxation time is determined by comparing the jetting of polymer solution from a Continuous Ink-Jet (CIJ) device experimentally and numerically. The numerical approach is first validated using test case and a viscoelastic Oldroyd-B model is then used to model the experimental solution. The relaxation time is then a parameter allowing us to fit numerical simulation onto experimental results. This mixed strategy is particularly convenient for weakly elastic solution for which physical parameters can not be measured using experimental rheometry setup.

1 Introduction

Capillary breakup phenomena have a wide range of applications from ink-jet printing to DNA sampling. In micro jetting devices, polymer solutions often experience non Newtonian behavior which greatly influence breakup dynamics. Drops generation from non Newtonian fluid jets breakup is a well known topic which has already been addressed both numerically and experimentally [1–3]. Elastic and viscous effects are known to have a great influence on the breakup dynamics. More precisely, they are known to delay the onset of the jet breakup [4, 5]. In the present work, the relaxation time of a weakly elastic ink used in industrial continuous ink-jet printing (CIJ) devices is determined. This ink is a low viscosity dilute polymer with high polydispersity. A first estimation of the elastic relaxation time is calculated using Zimm theory [6], and is found to be out of the measurement range of both extensional rheometry (ROJER [7]) or microfluidic devices [8]. As a result, an original approach is introduced to determine the relaxation time, relying on the comparison of both capillary breakup length and shapes between numerical simulations and experiments.

2 Experimental setup

The experimental device is similar to the one used for the ROJER extensional rheometry measurements [2] (see figure 1) and is commonly used in Continuous Ink-Jet process.

The flow is generated by a pump and the jet is created using a micro-nozzle. Then, it is strobed at a given frequency and synchronized with the drive frequency ($10kHz < f_d < 100kHz$) in order to display

a static image (1024×778 pixels with $1px \approx 1\mu m$). The visualization software is ImageXpert.

In the present work, the fluid jets have been generated experimentally with the same piezoelectric device at stimulation amplitudes ranging from 2V to 62V and with a constant dimensionless wave number $x = 0.6$, where x writes:

$$x = 2\pi R_0 \frac{v}{f} \quad (1)$$

with R_0 the radius of the unperturbed jet, v the jet velocity and f the stimulation frequency.

Reynolds and Ohnesorge numbers of the jet, are

$$Re = \rho v R_0 / \eta_0 = 110 \quad (2)$$

and

$$Oh = \eta_0 / \sqrt{\rho R_0 \sigma} = 0.2 \quad (3)$$

respectively. They are calculated for undisturbed jets and are constant for every disturbance amplitudes.

For high stimulation amplitude, we observe Fig.2 threads linking the first droplets to the unbroken jet which is typical of breakup of weakly elastic polymer strain hardening solutions [9].

Figure 2 depicts the jet morphologies after jetting the weakly elastic ink. The jets have been pictured at the breakup distance from the nozzle for stimulation amplitudes ranging from 2 to 62V. For small stimulation amplitude (left on the figure), drop shape remains almost the same in the linear regime of stimulation, i.e. where stimulation is lower than 15V. In that regime, we also observe a forward-merging satellite. For higher stimulation amplitude, no satellite can be observed anymore and a thread links first droplets to the unbroken jet. Typically, this thread is part of a breakup of weakly elastic polymer strain hardening solutions [9].

Figure 3 shows the breakup length as a function of the disturbance amplitude, i.e. as a function of the tension applied by the piezoelectric actuator. The so-called breakup length, also called "intact length" and noted \mathcal{L}_{exp}^b hereafter, has been widely studied both in linear and non-linear regime, (see [10] and therein references). It is directly linked to the nozzle outlet velocity disturbance [11, 12]. The transition between linear and non linear regimes is depicted by the change in breakup length slope and these regimes are predicted by the so-called linear and non-linear theories, respectively. A quasi-linear regime is thus observed for low amplitude stimulation (lower than 15V) and is in agreement with previous observations on drop shapes. As predicted by the theory, the breakup length decreases with the amplitude and seems to reach a minimum length for 62V and although the breakup lengths present an exponential decay, the regime below 15V will then be referred as linear regime hereafter.

2.1 Rheological characterization

Density $\rho = 873 \text{ kg.m}^{-3}$ and surface tension $\sigma = 22.8 \text{ mN.m}^{-1}$ of the fluid have been carefully measured using an DMA4500M device from Anton Paar and a MPT2 from Lauda companies, respectively.

The shear viscosity was measured using both ARG-2 from TA-Instruments, for low shear rates ($\dot{\gamma} < 1000 \text{ s}^{-1}$), and a m-VROC from RheoSense, for high shear rates ($1000 \text{ s}^{-1} < \dot{\gamma} < 10^6 \text{ s}^{-1}$). As can be seen on figure 4, viscosity shows a slight shear-thinning behavior around 10^6 s^{-1} , but too low to be considered if we consider measured uncertainties. For this reason, the fluid viscosity is assumed to be constant over the all full range of shear rate investigated here.

As stated in the previous section, the present ink is a weakly elastic polymer solution. Zimm theory [6] can thus be used to describe polymer relaxation dynamics considering hydrodynamic interactions between chains and solvent. Zimm's theory is based on an elastic dumbbell model: it takes into account the hydrodynamic interactions between solvent and polymers, but not the frictional interactions between chains. This theory particularly well adapted for dilute polymer solutions enables the calculation of a relaxation time τ_Z such as :

$$\tau_Z = \frac{\eta_s [\eta] M}{RT} = 0.4 \mu\text{s} \quad (4)$$

where η_s is the solvent viscosity in Pa.s , $[\eta]$ the intrinsic viscosity in $\text{m}^3.\text{kg}^{-1}$, M_w the polymer molec-

ular mass $kg.mol^{-1}$, R the universal gas constant and T the temperature in K .

τ_Z is an estimated, analytical relaxation time based onto main assumptions which are the monodispersity of polymer molecular weight distribution and solely hydrodynamic interactions between polymer chains and solvent. As in the present ink is unlikely to meet both criteria, and particularly the monodisperse assumption, the estimated relaxation time can only be considered as an order of magnitude of the real relaxation time.

Let us now consider the capillary time τ_c , given by :

$$\tau_C = \sqrt{\rho R_0^3 / \sigma} \quad (5)$$

with R_0 the unperturbed jet radius.

As the polymer relaxation time predicted by Zimm's theory is very small compared with the capillary time scale, the elasticity should have a negligible influence on the breakup dynamics for small to moderate stimulation amplitude. Moreover, this low relaxation $\tau_Z \ll \tau_C$ time prevent us from using the jetting device as a ROJER [7] in order to measure the relaxation time.

To the knowledge of the authors, no experimental device can capture such a short relaxation time and we follow another route in section 4 by comparing numerical simulation to experimental results in order to determine it. Firstly, numerical model were carefully assessed and calibrated in the next section using both a simple test case and simulations of a Newtonian fluid jet.

3 Validation of the numerical model

Computation were performed using OpenFoam® and more specifically with its multiphase solver interFoam [13]. In order to evaluate the ability of the solver to numerically model the jetting of a non-Newtonian fluid, it was first assessed on the well-known capillary instability growth of a Newtonian fluid. Moreover, jetting of Newtonian fluid were also considered.

3.1 Simulation of the capillary instability growth

The performance of the interFoam solver were assessed by simulating the growth of a perturbation at the surface of 2-dimensional axisymmetric Newtonian liquid column. Results were then compared to

$\rho_l(kg.m^{-3})$	1000
$\rho_g(kg.m^{-3})$	1
$\nu_l(Pa.s)$	10^{-3}
$\nu_g(Pa.s)$	10^{-6}
$h(m)$	$28 \cdot 10^{-4}$
$\lambda(m)$	$64 \cdot 10^{-4}$
$R_0(m)$	$7.07 \cdot 10^{-4}$
$\delta(m)$	$1.6 \cdot 10^{-5}$
Oh	0.2
$\tau_c(s)$	0.1
$\Delta_x(m)$	$7 \cdot 10^{-5}$

Table 1: Parameters of capillary instability simulations where the subscripts l and g stand for liquid and gaz, respectively.

the linear theory, initially derived by Rayleigh [4] and enhanced by Chandrasekhar [14], which provides well-known test cases [15, 16].

The analytical dispersion equation from [14] writes:

$$\gamma\tau_c = \sqrt{\frac{1}{2}(x^2 - x^4) + \frac{9}{4}Oh^2x^4} - \frac{3}{2}Ohx^2, \quad (6)$$

with γ the growth rate, τ_c the capillary time, x the dimensionless wave number and Oh the Ohnesorge number.

Simulation of the capillary instability growth consists in an axisymmetric flow within a rectangular domain of width λ and height h , and composed of a liquid of radius R_0 and a gaz. At $t = 0s$ the liquid is at rest and a small perturbation of wavelength λ and amplitude δ is applied to its surface. Domain is meshed with square elements of side Δ_x and simulation is found to converge with $\Delta_x < 7 \cdot 10^{-5}m$. Parameters of the simulation are summed up in Table 1 and Fig 5 which shows numerical results at different times $t \in [0s, 2s]$.

Comparison of theoretical growth rate from Eq. 6 with numerical results Fig. 6 shows an excellent

$\rho_l(kg.m^{-3})$	1128.88
$\nu_l(mPa.s)$	6.4
$\sigma(mN.m^{-1})$	69.16

Table 2: Physical parameters of glycerol + water solution.

agreement between analytical solution based onto linearized approach and the interFoam solver which compute solutions of the complete Navier-Stokes equation.

3.2 Numerical simulation of Newtonian CIJ

In order to fine tune the numerical model for CIJ cases, jetting of a Newtonian solution of water and glycerol is addressed. The experimental set-up is identical to the one that has been used to jet the weakly elastic ink in section 2.1. The density, viscosity and surface tension of the solution has been carefully measured using, respectively, an Anton Paar DMA4500, an Anton Paar Lovis 2000ME and a Lauda MPT-2. Table 2 sums up the physical properties of the solution used in the numerical simulation.

Figure 7(a-i) shows experimental jets pictured at the breakup distance from the nozzle for stimulation amplitudes ranging from 1 to 55V.

The numerical model of the CIJ device takes advantage of the axisymmetry of the problem so, the upper part of the numerical domain, is thus 2-dimensional. It includes fluid tank and nozzle as depicted in Fig. 8.

At $t = 0s$, both tank and nozzle are filled with fluid and the rest of the domain is filled with air. In order to jet the fluid, a pressure Dirichlet boundary condition is applied on the inlet of the domain (left side of the tank) such as:

$$P = P_{tank} + P_{stim} \cos(2\pi ft) \quad (7)$$

where P_{tank} and P_{stim} are related, respectively, to the absolute steady pressure in the fluid tank, driving the jetting velocity of the fluid, and the maximum stimulation pressure applied by the piezoelectric actuator. At the outlet, an outflow condition is applied.

To accurately determine P_{tank} , P_{stim} is set to zero, i.e. jetting an unperturbed jet of glycerol, and

both the mass flow and the dimensionless wave number x are experimentally measured and compared to numerical results by try and error process. In the present case the P_{tank} has been found to be $P_{tank} = 4140 \text{ mbar}$.

P_{stim} is directly related to the tension applied to the piezoelectric actuator and there is no direct relation between the amplitude of stimulation in Volt and the one in Pascal. In order to determine the pressure exerted on the fluid by the piezoelectric device, i.e. P_{stim} , as a function of the tension applied T_{stim} , we must compare experimental and numerical breakup jets. One way to do this link is to compare droplet shapes, but in this present case, and due to the high surface tension exhibited by the glycerol solution, the droplets created looks very similar (see Fig. 7). And hence, one can not be used as a criterion to discriminate jets. We then use the breakup lengths of the jets, respectively, \mathcal{L}_{exp}^b and \mathcal{L}_{num}^b , to assess the relation between P_{stim} and T_{stim} .

Figure 9 shows both \mathcal{L}_{exp}^b and \mathcal{L}_{num}^b and an excellent agreement can be found between P_{stim} and T_{stim} :

$$P_{stim} = 36.4 T_{stim}^{0.792} \quad (8)$$

It is worth pointing out that the numerical breakup length can strongly impacted by the mesh as \mathcal{L}_{num}^b relates to the length where fluid thread thickness tends towards zero. However the high surface tension exhibited by the glycerol solution prevent \mathcal{L}_{num}^b to diverge from \mathcal{L}_{exp}^b and an excellent agreement is found to be between them.

Droplet shapes depicted 10(a-c) shows also an excellent agreement between numerical and experimental results comprising satellites dynamic, which is also captured by the numerical model, from low (1.6V) to high amplitude stimulations (33V).

4 Numerical determination of the relaxation time

This section focuses on the determination of the relaxation time of the weakly elastic ink presented section 2.1. The numerical simulation is performed using the previously fine-tuned interFoam solver (see previous subsection 3.2) and the same 2D-axisymmetric geometry.

Neither shear thinning nor strain thickening behavior is expected, thus the Oldroyd-B viscoelastic model [17] is assumed to accurately describe viscoelastic behavior of the present weakly elastic ink. The equations governing the viscoelastic, incompressible, laminar flow are the mass conservation (Eq. 9) and the momentum balance (Eq. 10):

$$\nabla \cdot \mathbf{u} = 0 \quad (9)$$

$$\rho \left(\frac{\partial \mathbf{u}}{\partial t} \cdot \nabla \mathbf{u} \right) = -\nabla p + \nabla \cdot \boldsymbol{\tau} \quad (10)$$

where \mathbf{u} is the velocity vector, t is the time, p is the pressure and $\boldsymbol{\tau}$ is the total stress tensor. The total stress can be split in a solvent contribution (τ_s) and a polymeric contribution (τ_p), such as $\boldsymbol{\tau} = \tau_s + \tau_p$, and

$$\tau_s = \eta_s (\nabla \mathbf{u} + \nabla \mathbf{u}^T) \quad (11)$$

with η_s the solvent viscosity.

For the Oldroyd-B model, the polymeric stress writes

$$\tau_p + \lambda \overset{\nabla}{\tau}_p = \eta_p (\nabla \mathbf{u} + \nabla \mathbf{u}^T) \quad (12)$$

with λ the relaxation time, $\overset{\nabla}{\tau}_p$ the upper-convected derivative of τ_p and η_p the polymeric viscosity.

The solvent and polymer contribution to viscosity, respectively $\eta_s = 1.2 \text{ mPa.s}$ and $\eta_p = 3.75 \text{ mPa.s}$.

Although the nozzle geometry is a property of Markem-Image© and can not be disclosed, a complete study of its geometry was carried out using a SEM (see Fig. 11) to get its exact dimensions.

Hereafter, the influence of the relaxation time τ_e onto the breakup shape is investigated. Giving the value $\tau_Z = 0.4\mu s$ found in section 2.1 using Zimm's theory, τ_e from $0.5\mu s$ to $1\mu s$ will be tested.

The relaxation time has an influence on the average jet velocity v : the more elastic is the fluid, the slower is the jet. Thus, the instability wave number x (see 1) increases when τ_e increases. Consequently P_{tank} depends on τ_e and has been determined by ensuring a constant dimensionless wave number $x = 0.6$ for unperturbed viscoelastic jets (i.e. setting $P_{stim} = 0$ in eq. 7). Figure 12 shows the linear relation found between P_{tank} and the fluid relaxation time in order to get $x = 0.6$.

It is worth pointing out that over the studied range of relaxation times, the jet does not exhibit die-swell effect at the nozzle exit : the dependence of R_0 with τ_e is then assumed negligible, and, consequently, P_{tank} only influences the value of the jet averaged velocity v . Moreover Figure 13 presents the axial velocity profile at the nozzle outlet obtained for $\tau_e = 0\mu s$ (Newtonian), $\tau_e = 0.5\mu s$ and $\tau_e = 1\mu s$ for a jet without disturbance. It seems that within the studied relaxation time range, elasticity has a small influence onto velocity profiles.

From now on, a disturbance is applied to the jet using the pressure boundary condition (see eq. 7). In order to compare the numerical results to the experimental ones, one must find the relation between P_{stim} and V_{stim} , which denote, respectively, the numerical and experimental disturbance amplitudes. In section 3.2, the correlation has been found based on the breakup length.

However, as previously stated, the breakup length criterion is not fully appropriate for low to moderate surface tension fluids as the mesh has an outstanding influence on it. The results are thus compared using both the breakup length and the breakup shape which, the later being far less influenced by the mesh and thus is a good additional criterion.

For each numerical fluid, i.e. Newtonian and Oldroyd-B with $\tau_e \in \{0.5, 0.75, 0.85, 1\}$, calculations are made for two values of P_{stim} , $P_{stim} = 0.3 \cdot P_{tank}$ and $P_{stim} = 0.5 \cdot P_{tank}$.

Figure 14 presents results obtained for $P_{stim} = 0.3 \cdot P_{tank}$ for every numerical fluid and with the best experimental math. From these first results, either $\tau_e = 0.75\mu s$ or $\tau_e = 0.85\mu s$ are potential candidates by matching the best experimental drop shape obtained with a disturbance amplitude of $54.5V$. While results lie in the non linear regime (see Fig. 3) the influence of the relaxation time has a moderate effect onto the drop shapes.

However when comparing the breakup length $\mathcal{L}_b^{0.3}$ we observe a strong influence of the relaxation

time and, as expected, some discrepancies between the candidates and the experimental lengths which are shorter.

Figure 15 presents results for $P_{stim} = 0.3 \cdot P_{tank}$. In this case, the Newtonian case and the Oldroyd-B model at $\tau_e = 0.5\mu s$ both exhibit significant shape differences compared to the experimental case. The computation for $\tau_e = 1\mu s$ is not presented as a breakup inversion occurs, and as a result, the jet breaks up outside the numerical domain, i.e. at a length greater than $6.5mm$. Again, relation time of $\tau_e = 0.75\mu s$ and $\tau_e = 0.85\mu s$ give the most accurate breakup shapes, as already observed for $P_{stim} = 0.3 \cdot P_{tank}$.

Small differences between numerical and experimental drop shapes may due both to non linear viscoelastic effects that are not taken into account in the Oldroyd-B model and experimental uncertainties.

Fluids	$\mathcal{L}_b^{0.3} (mm)$	$\mathcal{L}_b^{0.5} (mm)$
Experimental	3.28	2.29
Newtonian	2.85	2.54
$\tau_e = 0.5\mu s$	3.3	2.25
$\tau_e = 0.75\mu s$	3.95	2.85
$\tau_e = 0.85\mu s$	4.45	4.25
$\tau_e = 1\mu s$	5.5	> 6.5

Table 3: Breakup lengths $\mathcal{L}_b^{0.3}$ and $\mathcal{L}_b^{0.5}$ of the numerical and experimental fluids.

As we can see, small changes in the polymer relaxation time τ_E have a great influence on the breakup morphology of Rayleigh-Plateau jet instability.

The present work allowed us to determine a tiny range for the longest relaxation time with a precision of $10^{-7}s$. The numerically measured relaxation time $\tau_e = 0.75 - 0.85\mu s$ is coherent with Zimm predictions even if it is slightly higher ($\tau_z = 0.4\mu s$). The small difference between analytical and computational results may due to polydispersity of the polymer solution as τ_z is calculated using the averaged molecular mass M_w . Although some polymer chains in the present solution have higher molecular mass which increases the solution relaxation time.

5 Conclusion

This original approach allows to determine the rheological properties of low viscosity and weakly viscoelastic polymer solution that can not be addressed by any experimental measurement method. Based on a trial-and-error technique. It relies on the strong dependency of the pinching curvature onto the viscoelastic relaxation time at high disturbance amplitude. However, this approach rely on an accurate numerical description of the physics at play in the process. The rheological model used must be carefully chosen to adequately model the experimental fluid.

6 Acknowledgements

The authors thank Markem-Imaje©, a Dover® company, for their ongoing financial support, nozzle manufacture and CIJ expertise.

The Laboratoire Rhologie et Procds is part of the LabEx Tec 21 (Investissements d’Avenir - grant agreement n°ANR-11-LABX-0030) and of the PolyNat Carnot Institut (Investissements d’Avenir - grant agreement n°ANR-11- CARN-030-01).

References

- [1] Morrison, N. F., and Harlen, O. G., 2011. “Inkjet printing of non-newtonian fluids”. In NIP & Digital Fabrication Conference, Vol. 2011, Society for Imaging Science and Technology, pp. 360–364.
- [2] Rodríguez-Rivero, C., Del Valle, E. M., and Galán, M. A., 2015. “Experimental and linear analysis for the instability of non-newtonian liquid jets issuing from a pressurized vibrating nozzle”. *AIChE Journal*, **61**(6), pp. 2070–2078.
- [3] McIlroy, C., Harlen, O., and Morrison, N., 2013. “Modelling the jetting of dilute polymer solutions in drop-on-demand inkjet printing”. *Journal of Non-Newtonian Fluid Mechanics*, **201**, pp. 17–28.
- [4] Rayleigh, L., 1892. “Xvi. on the instability of a cylinder of viscous liquid under capillary force”. *The London, Edinburgh, and Dublin Philosophical Magazine and Journal of Science*, **34**(207), pp. 145–154.
- [5] Gordon, M., Yerushalmi, J., and Shinnar, R., 1973. “Instability of jets of non-newtonian fluids”. *Transactions of The Society of Rheology (1957-1977)*, **17**(2), pp. 303–324.

- [6] Zimm, B. H., 1956. “Dynamics of polymer molecules in dilute solution: viscoelasticity, flow birefringence and dielectric loss”. *The journal of chemical physics*, **24**(2), pp. 269–278.
- [7] Keshavarz, B., Sharma, V., Houze, E. C., Koerner, M. R., Moore, J. R., Cotts, P. M., Threlfall-Holmes, P., and McKinley, G. H., 2015. “Studying the effects of elongational properties on atomization of weakly viscoelastic solutions using rayleigh ohnesorge jetting extensional rheometry (rojer)”. *Journal of Non-Newtonian Fluid Mechanics*, **222**, pp. 171–189.
- [8] Galindo-Rosales, F. J., Alves, M., and Oliveira, M. S., 2013. “Microdevices for extensional rheometry of low viscosity elastic liquids: a review”. *Microfluidics and nanofluidics*, **14**(1-2), pp. 1–19.
- [9] Christanti, Y., and Walker, L. M., 2002. “Effect of fluid relaxation time of dilute polymer solutions on jet breakup due to a forced disturbance”. *Journal of Rheology (1978-present)*, **46**(3), pp. 733–748.
- [10] Eggers, J., and Villermaux, E., 2008. “Physics of liquid jets”. *Reports on progress in physics*, **71**(3), p. 036601.
- [11] Pimbley, W., and Lee, H., 1977. “Satellite droplet formation in a liquid jet”. *IBM Journal of Research and Development*, **21**(1), pp. 21–30.
- [12] Rosello, M., Maîtrejean, G., Roux, D. C., Jay, P., Barbet, B., and Xing, J., 2018. “Influence of the nozzle shape on the breakup behavior of continuous ink jets”. *Journal of Fluids Engineering*, **140**(3).
- [13] Deshpande, S. S., Anumolu, L., and Trujillo, M. F., 2012. “Evaluating the performance of the two-phase flow solver interfoam”. *Computational science & discovery*, **5**(1), p. 014016.
- [14] Chandrasekhar, S., 2013. *Hydrodynamic and hydromagnetic stability*. Courier Corporation.
- [15] Delteil, J., Vincent, S., Erriguible, A., and Subra-Paternault, P., 2011. “Numerical investigations in rayleigh breakup of round liquid jets with vof methods”. *Computers & Fluids*, **50**(1), pp. 10–23.
- [16] Cervone, A., Manservigi, S., and Scardovelli, R., 2010. “Simulation of axisymmetric jets with a finite element navier–stokes solver and a multilevel vof approach”. *Journal of Computational Physics*, **229**(19), pp. 6853–6873.
- [17] Oldroyd, J., 1950. “On the formulation of rheological equations of state”. In *Proceedings of the Royal Society of London A: Mathematical, Physical and Engineering Sciences*, Vol. 200, The Royal Society, pp. 523–541.

List of Figures

1	15
2	Breakup shapes of the polymer solution for stimulation amplitudes ranging from 2V (left) to 62V (right).	16
3	Experimental breakup lengths \mathcal{L}_{exp}^b for the weak elastic ink studied in the present work. The 15V stimulation amplitude is depicted by the dashed line.	17
4	Dynamic viscosity of the present polymer solution as a function of the shear rate. . . .	18
5	Evolution of the capillary instability (liquid in red and gaz in blue)	19
6	Growth rate $\gamma\tau_c$ as a function of of the dimensionless wave number x	20
7	Experimental jets for different stimulation amplitude (in Volts) located a the breakup length.	21
8	Converged mesh of the tank, nozzle and nozzle outlet of the axisymmetric numerical model.	22
9	Numerical and Experimental breakup lengths for glycerol solution.	23
10	Comparison between experimental (black and white) and numerical (colour) droplet shapes for different amplitudes of stimulation.	24
11	Image of the present nozzle obtained by SEM.	25
12	P_{tank} as function of τ_e ensuring a constant dimensionless wave number $x = 0.6$ for unperturbed viscoelastic jets.	26
13	Computational axial velocity profiles at the nozzle exit for the Newtonian and Oldroyd-B ($\tau_e = 0.5\mu s$ and $\tau_e = 1\mu s$) fluid jets.	27
14	Breakup shapes for $P_{stim} = 0.3 \cdot P_{tank}$ for both experimental (black) and numerical (red) fluids.	28
15	Breakup shapes for $P_{stim} = 0.5 \cdot P_{tank}$ for both experimental (black) and numerical (red) fluids.	29

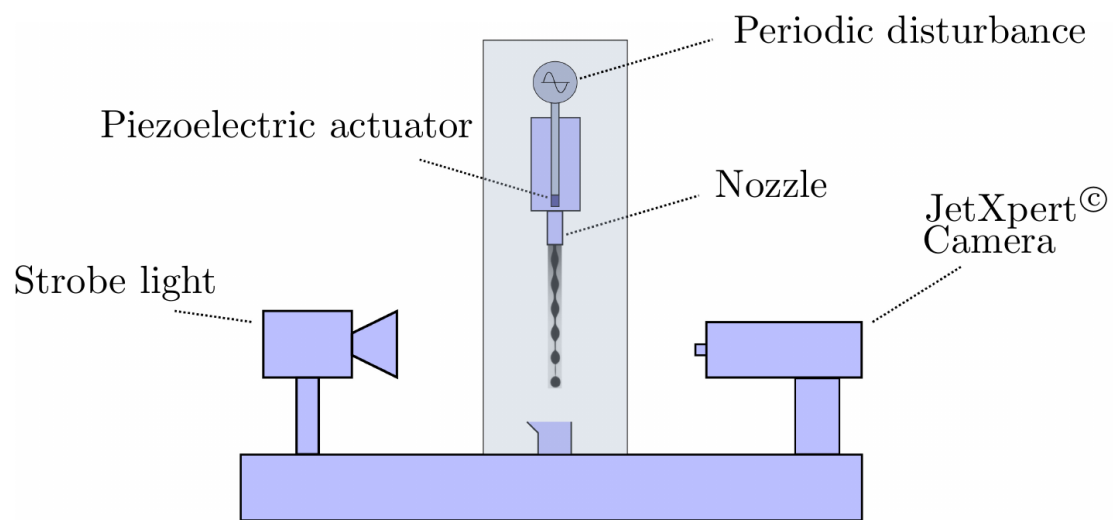


Fig. 1

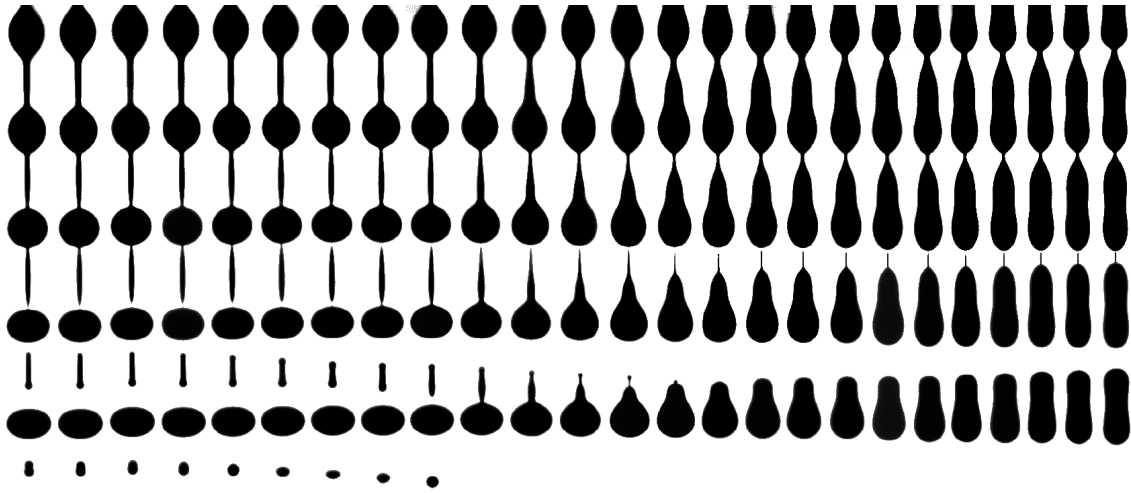


Fig. 2: Breakup shapes of the polymer solution for stimulation amplitudes ranging from 2V (left) to 62V (right).

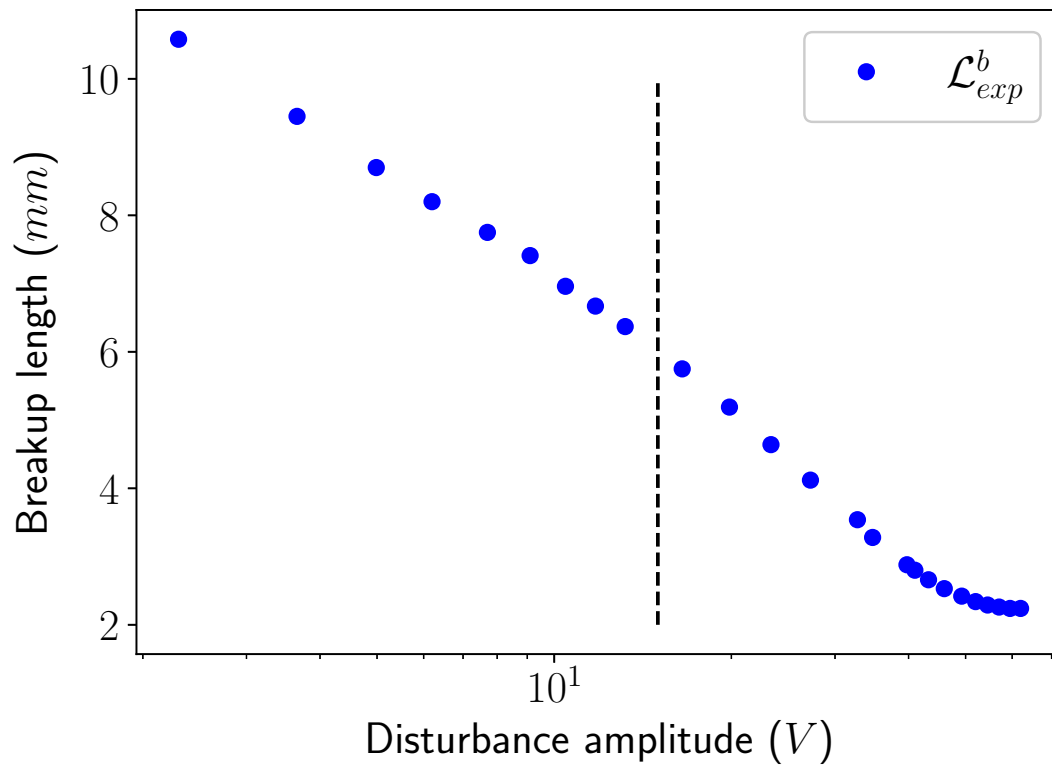


Fig. 3: Experimental breakup lengths \mathcal{L}_{exp}^b for the weak elastic ink studied in the present work. The 15V stimulation amplitude is depicted by the dashed line.

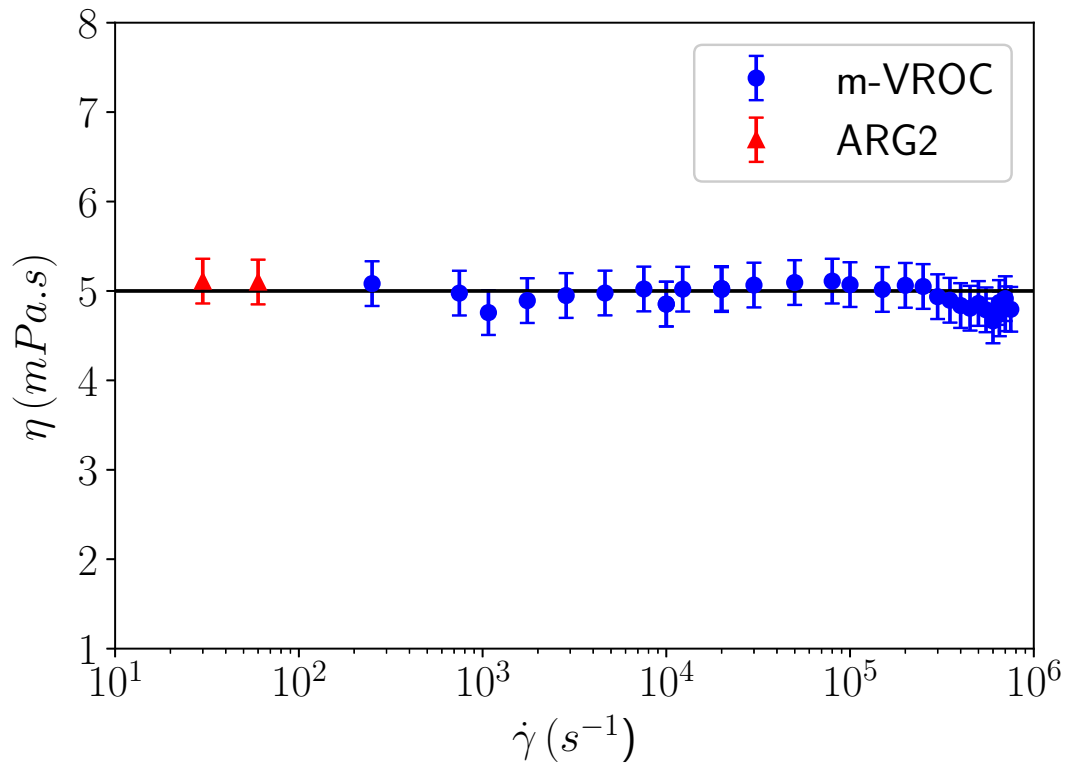


Fig. 4: Dynamic viscosity of the present polymer solution as a function of the shear rate.

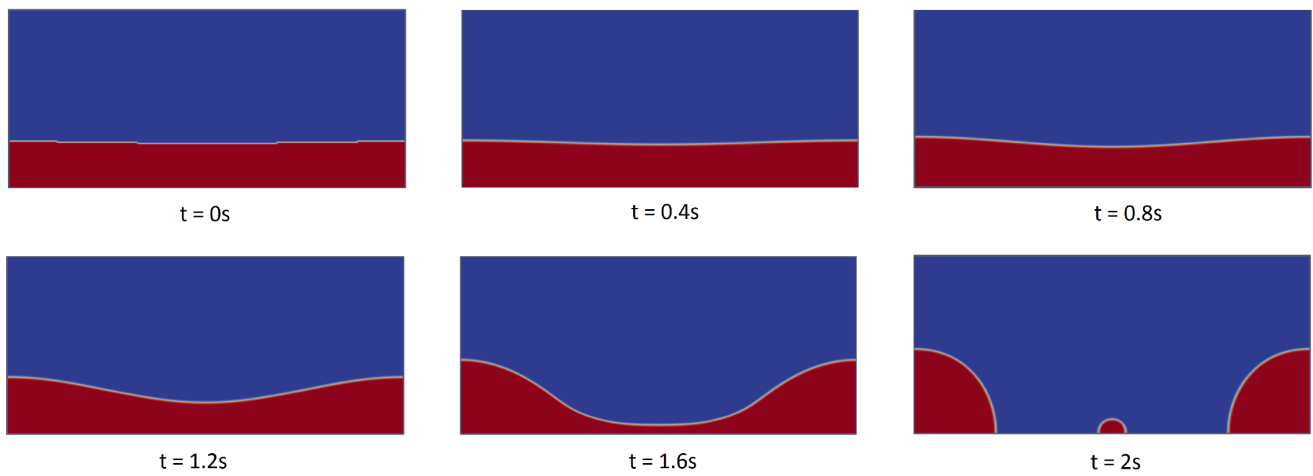


Fig. 5: Evolution of the capillary instability (liquid in red and gaz in blue)

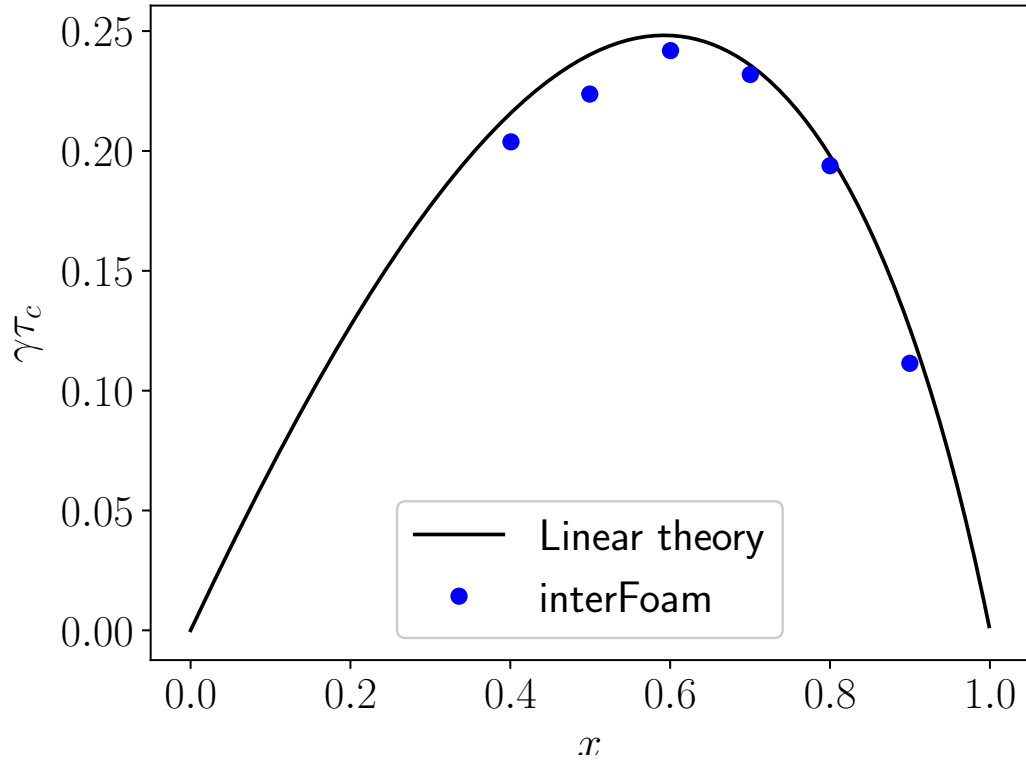


Fig. 6: Growth rate $\gamma\tau_c$ as a function of of the dimensionless wave number x

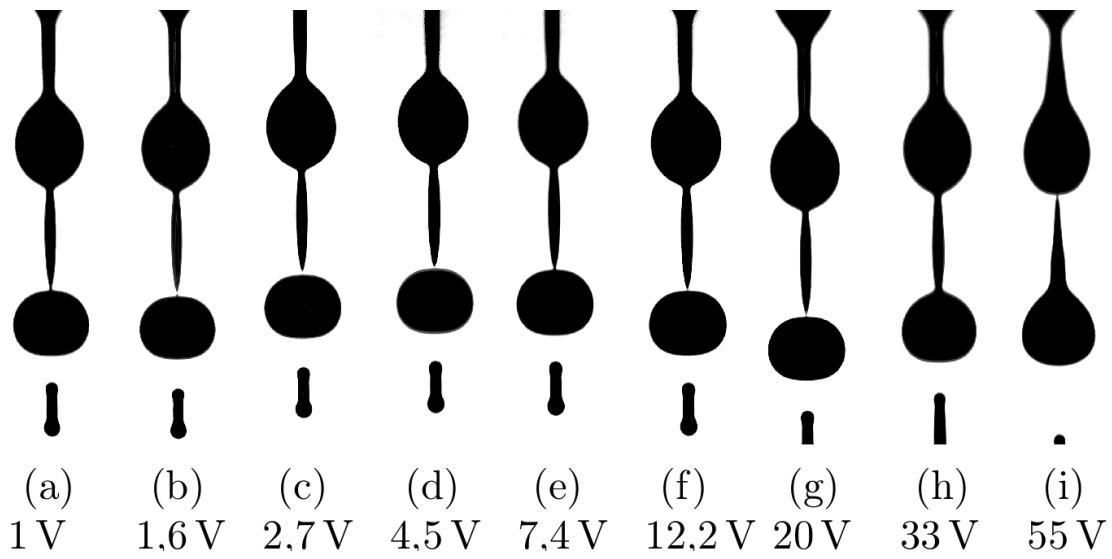


Fig. 7: Experimental jets for different stimulation amplitude (in Volts) located a the breakup length.

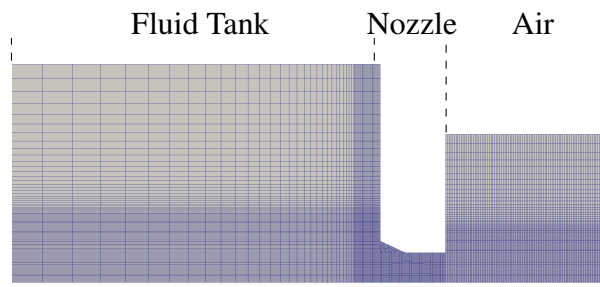


Fig. 8: Converged mesh of the tank, nozzle and nozzle outlet of the axisymmetric numerical model.

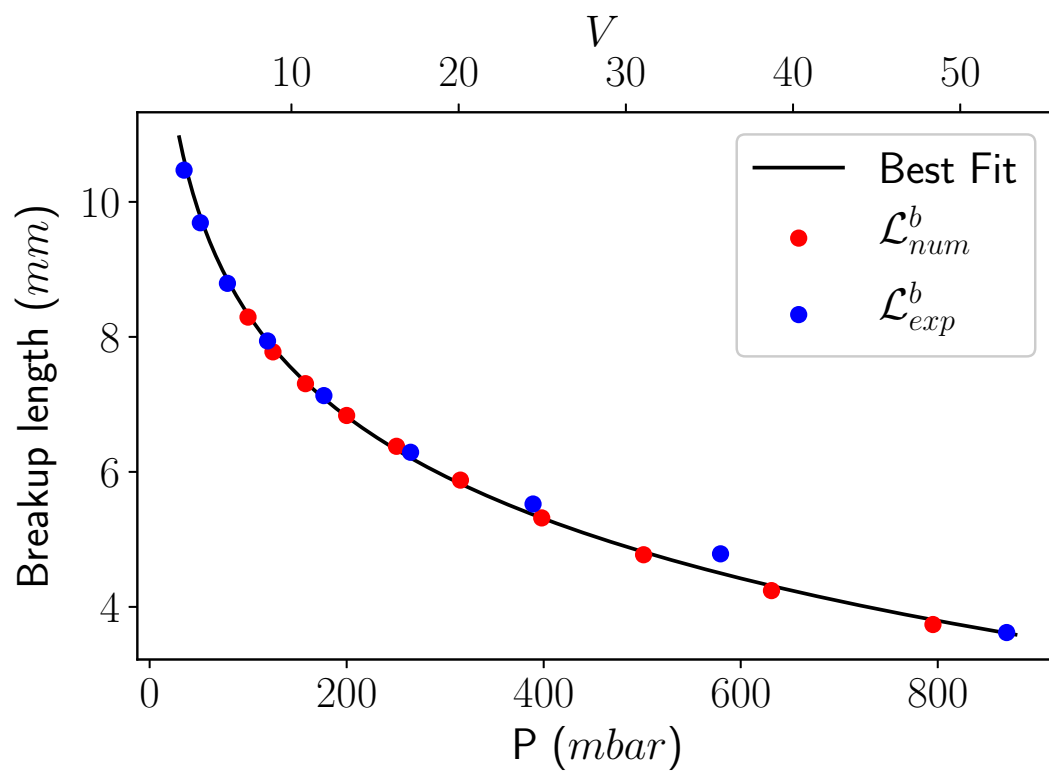
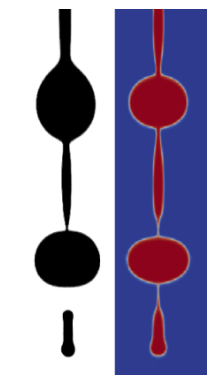
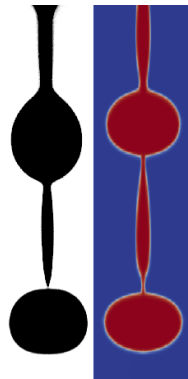


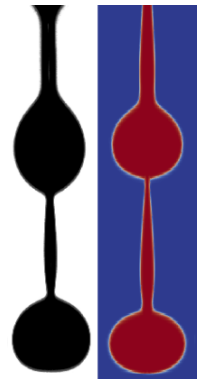
Fig. 9: Numerical and Experimental breakup lengths for glycerol solution.



(a) 1.6V -
53mbar



(b) 12.2V -
264mbar



(c) 33V -
580mbar

Fig. 10: Comparison between experimental (black and white) and numerical (colour) droplet shapes for different amplitudes of stimulation.

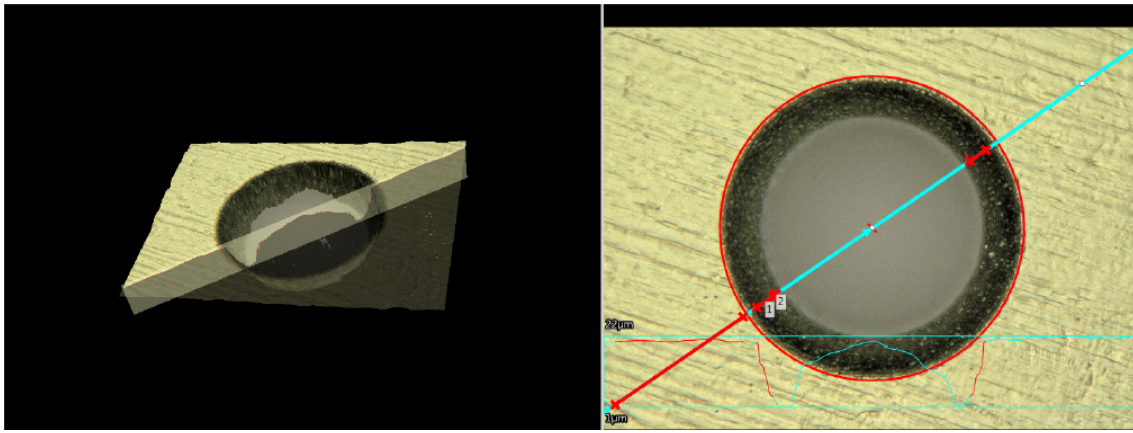


Fig. 11: Image of the present nozzle obtained by SEM.

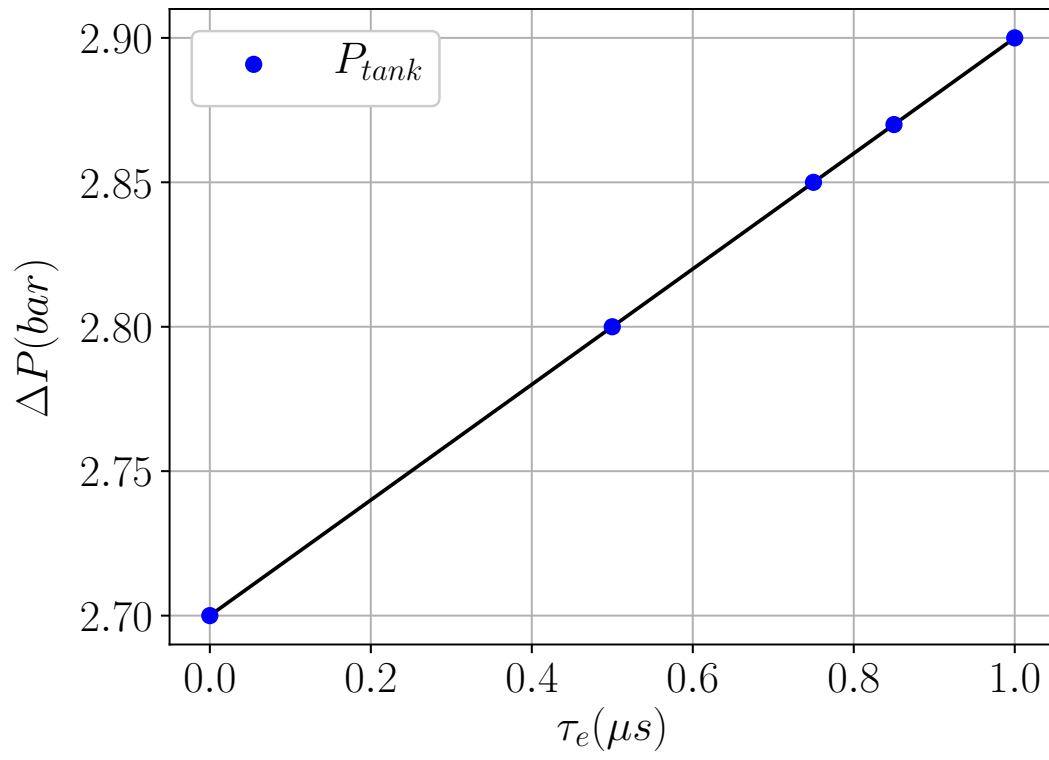


Fig. 12: P_{tank} as function of τ_e ensuring a constant dimensionless wave number $x = 0.6$ for unperturbed viscoelastic jets.

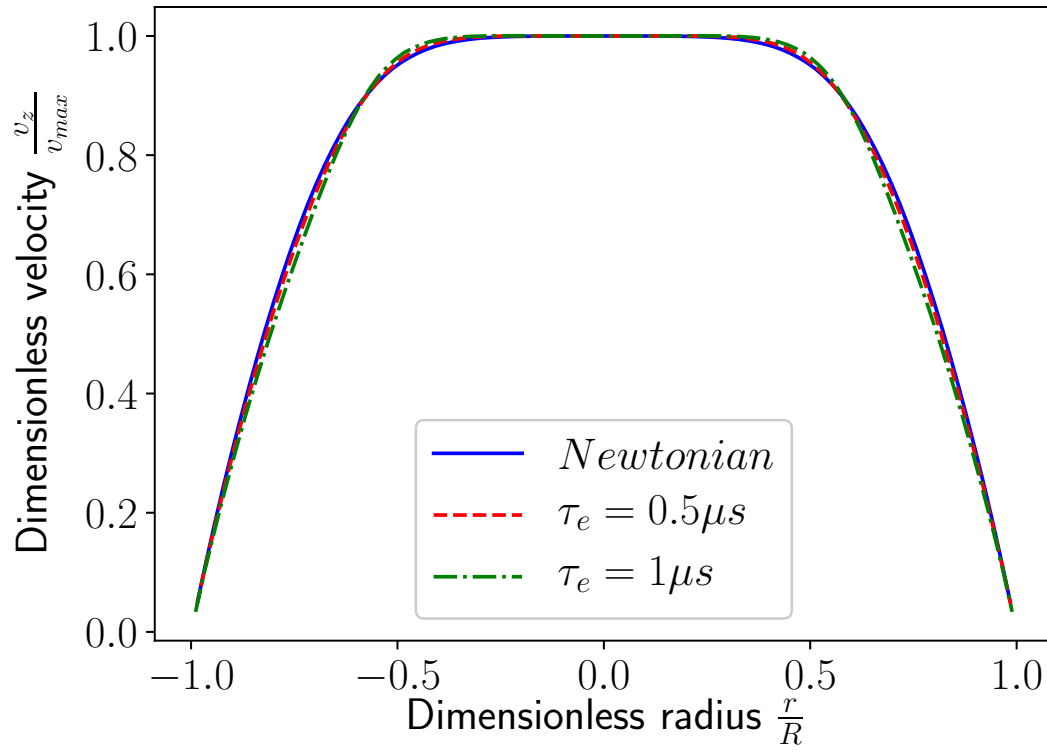


Fig. 13: Computational axial velocity profiles at the nozzle exit for the Newtonian and Oldroyd-B ($\tau_e = 0.5\mu s$ and $\tau_e = 1\mu s$) fluid jets.

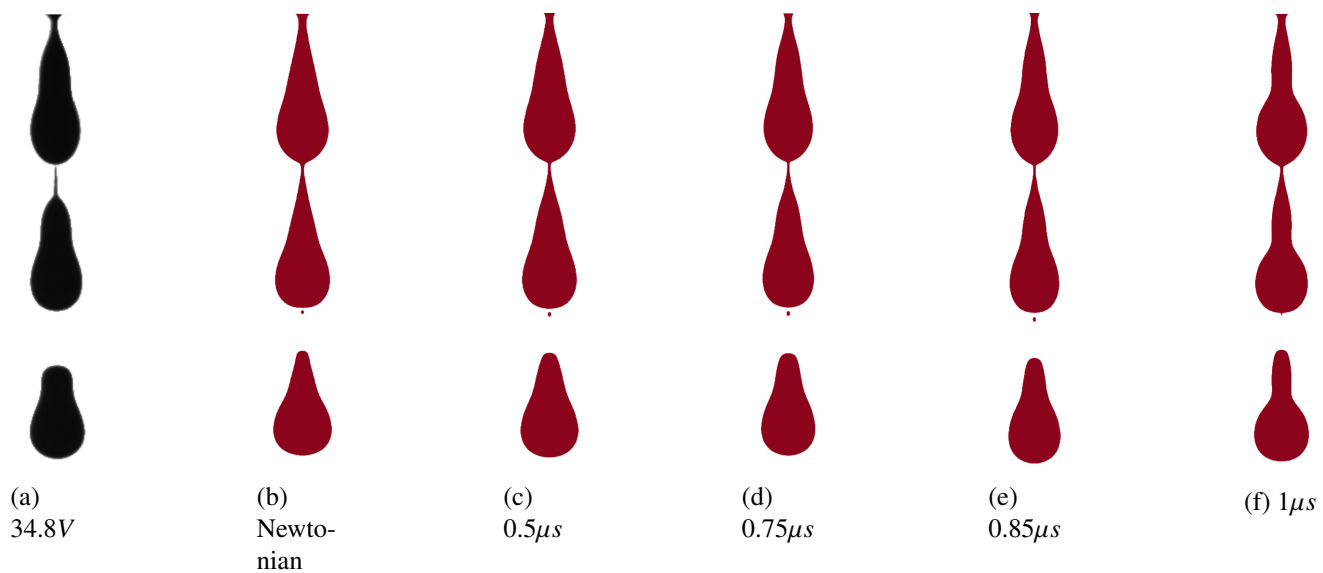


Fig. 14: Breakup shapes for $P_{stim} = 0.3 \cdot P_{tank}$ for both experimental (black) and numerical (red) fluids.

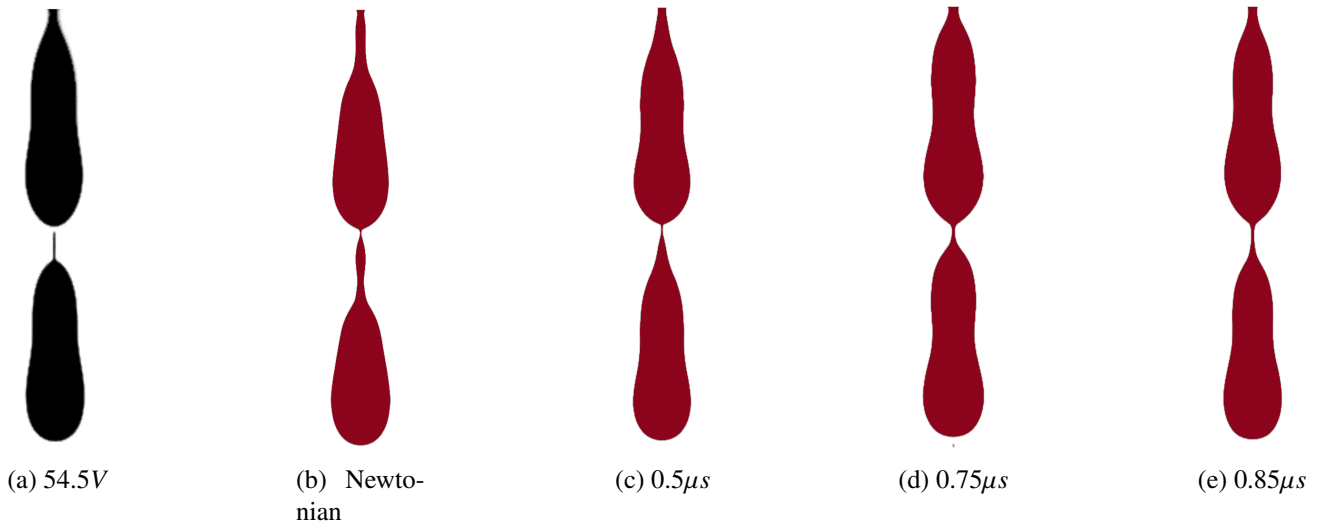


Fig. 15: Breakup shapes for $P_{stim} = 0.5 \cdot P_{tank}$ for both experimental (black) and numerical (red) fluids.